PCCP

Accepted Manuscript

ROYAL SOCIETY OF CHEMISTRY

www.rsc.org/pccp

How exciton-vibrational coherences control charge separation in the photosystem II reaction center

Vladimir I. Novoderezhkin,*[a] Elisabet Romero,[b] and Rienk van Grondelle[b]

[a]A. N. Belozersky Institute of Physico-Chemical Biology, Moscow State University, Leninskie Gory, 119992, Moscow, Russia; e-mail: novoder@belozersky.msu.ru;
[b]Department of Biophysics, Faculty of Sciences, VU University Amsterdam, De Boelelaan 1081, 1081 HV Amsterdam, The Netherlands.
** To whom correspondence should be addressed*

†Electronic supplementary information (ESI) available

Abstract

In photosynthesis absorbed sun light produces collective excitations (excitons) that form a coherent superposition of electronic and vibrational states of the individual pigments. Two-dimensional (2D) electronic spectroscopy allows a visualization of how these coherences are involved in the primary processes of energy and charge transfer. Based on quantitative modeling we identify the exciton-vibrational coherences observed in 2D photon echo of the photosystem II reaction center (PSII-RC). We find that the vibrations resonant with the exciton splittings can modify the delocalization of the exciton states and produce additional states, thus promoting directed energy transfer and allowing a switch between the two charge separation pathways. We conclude that the coincidence of the frequencies of the most intense vibrations with the splittings within the manifold of exciton and charge-transfer states in the PSII-RC is not occurring by chance, but reflects a fundamental principle of how energy conversion in photosynthesis was optimized.

1. Introduction

In photosynthesis solar light is absorbed by light-harvesting complexes from where the excitation energy is transferred to the reaction center (RC) where a charge separation occurs.[1–3] In photosynthetic light-harvesting and reaction center complexes the individual excited states of pigments (absorbing molecules) can be coherently mixed depending on their transition energies (that are randomly modulated by conformational disorder). When the energy gap between any pair of pigments is less than the interaction energy between them, the pigments become excitonically coupled, producing delocalized states with extremely fast exciton relaxation between them. In this way the energy can be quickly transferred between separated areas of a photosynthetic complex through such strongly coupled (or coherently 'wired') chains of pigments. Conformational motion can create and destroy such chains, thus directing the energy flow into different channels, depending on the realization of the energetic disorder. In RCs the excited states of the pigments can also be strongly mixed with charge-transfer (CT) states.[4,5] This allows the formation of channels with fast and effective electron transfer pathways.[6]

In 2D electronic spectroscopy[7] the existence of strongly coupled pigment chains can be visualized by the coherent excitation of the corresponding exciton states.[8-10] If any pair of states contains a mixing of pigments, then their coherent excitation will produce visible oscillations in the 2D responses. In this way the dynamic coherence between the eigenstates created by impulsive laser excitation highlights the inner coherence (that is the coherent mixing of the pigments within eigenstates). It is important to realize that such inner coherence is responsible for a directed and effective energy transfer also upon non-coherent excitation as it occurs in natural photosynthesis.

In addition to electronic coherences, the measured 2D kinetics usually contains many oscillatory features due to vibrational coherences. In order to distinguish between the excitonic and vibrational coherences it is useful to analyze the Fourier-transformed (2DFT) maps (also called 2D frequency maps) showing the distribution of oscillating amplitudes at any fixed frequency.[11] Quantitative modeling of the 2DFT maps measured for the dimeric subunit B820 of the bacterial LH1 antenna, allowed us to separate the contributions of different types of coherences, that is purely vibrational, mixed exciton-vibrational, and predominantly excitonic coherences.[11]

In this paper we model the 2DFT maps measured for the isolated reaction center of photosystem II (PSII-RC). Preliminary analysis of these maps suggested the mixed (exciton-vibrational) character of the coherences and provided evidence for the involvement of resonant intra-pigment vibrational modes (that is modes resonant with the exciton and exciton-CT splittings) in the energy transfer and primary charge separation events.[6] Notice that modeling of the 2DFT maps of the PSII-RC has been recently performed using a simplified model including only two pigments (the special pair P_{D1} and P_{D2}).[12] This model allowed only a partial explanation of the maps at frequencies close to the exciton splitting within the special pair, and, in addition, fails to explain 2DFT maps at other frequencies, in particular the 120 cm^{-1} map containing coherent excitation of the levels with contribution from other pigments. In the present modeling we use the exciton–vibrational model of the PSII-RC containing the 4 pigments from the active branch directly involved in charge separation. Such a reduced model still contains all the essential exciton splittings, making it possible to reproduce a large part of the observed 2DFT maps.

Based on this 4-state model we classify the exciton-vibrational coherences existing in the PSII-RC and explore the influence of resonant vibrations on energy and electron transfers. It is worth noting that the role of vibrations in light harvesting has attracted much interest in recent work.[13-22] In present study we demonstrate that resonant vibrations can change the exciton structure of RC and can induce the switching between different pathways of charge separation. Our modeling shows that the PSII-RC is a beautiful example of a solar energy converting device where vibrations play a special role by promoting directed energy and electron transfers (both in a femtosecond laser experiment and in natural photosynthesis).

2. Results

Exciton structure of PSII-RC.

In this paper we use a 4-state model (see Methods) that includes the pigments from the active branch of the PSII RC, that is the special pair chlorophylls P_{D1} and P_{D2}, the accessory chlorophyll Chl_{D1}, and the pheophytin Phe_{D1}. Such a model yields an exciton structure that mimics the structure appearing in the full exciton model (including the 8 pigments and 4 CT states present in the RC),[4] as shown in Figure 1. In particular, the model contains all essential exciton splittings with the same relative intensities of the absorption components as in the full model. The lowest level is largely localized on the red-most $\mathrm{Chl}_{\mathrm{D1}}$. The second one (lying 116 cm^{-1} higher) is the lowest level of the special pair $\mathrm{P}_{\mathrm{D1}}\mathrm{P}_{\mathrm{D2}}$ with some admixture of $\mathrm{Phe}_{\mathrm{D1}}$. The third level (that is only 26 cm^{-1} higher than the second one) has the same structure, but with smaller contribution of the special pair and a larger participation of $\mathrm{Phe}_{\mathrm{D1}}$. The fourth level is the higher level of special pair. The four pigments included into the reduced model participate into the lowest exciton state of the full model acting as the primary donor, i.e. initiating the charge separation from $\mathrm{Chl}_{\mathrm{D1}}$. These pigments are also involved into the second channel of charge separation starting from the special pair (mixed with the $\mathrm{P}_{\mathrm{D2}}{}^{+}\mathrm{P}_{\mathrm{D1}}{}^{-}$ level).[24,25] This second channel dominates in the realizations of the disorder, where the $\mathrm{P}_{\mathrm{D1}}\mathrm{P}_{\mathrm{D2}}\rightarrow\mathrm{P}_{\mathrm{D2}}{}^{+}\mathrm{P}_{\mathrm{D1}}{}^{-}$ relaxation is faster than population of the red-most $\mathrm{Chl}_{\mathrm{D1}}$ (as shown in numerical examples in ref. 6).

Exciton-vibrational eigenstates, ground-state absorption (OD) spectra.

In this section we explore the exciton-vibrational (vibronic) structure of the ground-state absorption (OD) spectra in the case of coupling to a single vibrational mode with frequency Ω=120, 340, or 740 cm^{-1}. In the low-temperature limit (see Methods) the components of OD can be numbered by the index b of one-exciton vibronic states. Parameters of the transitions from the ground to the vibronic states b are listed in Tables S1-S3 (see ESI†). The OD spectrum is most simple when the vibrational frequency Ω significantly exceeds all the exciton splittings (including the biggest one, that equals to 436 cm^{-1} in the absence of disorder), as shown in Figure 2, corresponding to Ω=740 cm^{-1}.

In the absence of coupling (Δ=0) the spectrum consists of four pure exciton transitions (Figure 2), that is, the same as shown in Figure 1. Here we label these zero-phonon levels (ZPL), corresponding to b=1-4 as 1^{Chl}, 2^{P1P2}, 3^{Phe}, and 4^{P1P2}, respectively. In the presence of coupling the diabatic states become displaced along the nuclear coordinates and their mixing produces excitonic ZPLs that are shifted with respect to ZPLs at Δ=0. In particular, for coupling to the vibrational mode Ω=740 cm^{-1}, this shifting changes the order of the second and third levels (Figure 2). The sequence of ZPLs is now 1^{Chl}, 2^{Phe}, 3^{P1P2}, and 4^{P1P2}. Higher vibronic states (b>4) include 4 vibrational satellites of the 1^{Chl} state, (we denote them as $\{b^1\}=5^1, 6^{1\mathrm{m}}, 7^1$, or 8^1), 4 satellites of the 2^{Phe} state ($\{b^2\}=9^2, 10^{2\mathrm{m}}, 11^2, 12^2$), 4 satellites of the 3^{P1P2} state ($\{b^3\}=13^3, 14^{3\mathrm{m}}, 15^3, 16^3$), and 4 satellites of the 4^{P1P2} state ($\{b^4\}=17^4, 18^4, 19^{4\mathrm{m}}, 20^4$). Superscript 'm' labels the states with the wavefunctions oriented along the so-called 'magic' direction, corresponding to the correlated nuclear motion (see Methods). It is interesting to note that the splitting within the $\{b^1\}$ and $\{b^2\}$ manifolds (associated with the quasi-localized ZPLs) is relatively small, whereas the $\{b^3\}$ and $\{b^4\}$ sub-bands (associated with the two excitonic origins of the special pair) contain levels 16^3 and 17^4 reflecting a nontrivial interplay of the electronic and vibrational motion induced by strong exciton coupling within the special pair. In particular, the energy of these states is significantly different from the energy of the pure vibrational sublevels 13^3-15^3 and 18^4-20^4.

Figure 3 shows the OD spectrum for coupling to the vibrational mode Ω=340 cm^{-1}, when the vibrational frequency is in quasi-resonance with the exciton splitting within the special pair $\mathrm{P}_{\mathrm{D1}}\mathrm{P}_{\mathrm{D2}}$. In the absence of coupling (Δ=0) the spectrum consists again of four ZPLs, that is 1^{Chl}, 2^{P1P2}, 3^{Phe}, and 8^{P1P2}, respectively (the vibrational satellites of the first level 4^1-7^1 are now lying below the fourth ZPL, that should be labeled as 8^{P1P2}). In the presence of coupling the order of ZPLs is 1^{Chl}, 2^{Phe}, 3^{P1P2}, and 4^{P1P2} (the fourth ZPL is shifted to the red below the vibrational sub-levels, and should be labeled as 4^{P1P2}). The vibrational sub-bands $\{b^1\}$-$\{b^4\}$ look very similar to the Ω=740 cm^{-1} case (Figure 2), but the 17^4 level (reflecting a specific exciton-vibrational mixing within the special pair) is relatively more intense, borrowing almost a half of the dipole strength of the original 8^{P1P2} ZPL. So, the resonant vibration splits the 8^{P1P2} ZPL into a new red-shifted 4^{P1P2} ZPL and the additional pseudo-ZPL 17^4 level. To highlight this difference between the 17^4 level and other (usual) vibrational satellites, we label the latter as $17^{4\mathrm{z}}$. Another difference is that the non-resonant 17^4 level is characterized by equal participation from P_{D1} and P_{D2}, whereas the $17^{4\mathrm{z}}$ level is predominantly localized at P_{D1} (see Tables S1 and S2).

Figure 4 shows the OD spectrum for coupling to the vibrational mode Ω=120 cm^{-1}, when the vibrational frequency is in quasi-resonance with the exciton splitting between the lowest ZPL and the second and third ZPLs. In the absence of coupling (Δ=0) the lowest eigenstates are: 1^{Chl} and 2^{P1P2} ZPLs and four forbidden vibrational satellites of the 1^{Chl} state ($\{b^1\}=3^1, 4^1, 5^1, 6^1$). The next allowed state is 7^{Phe} ZPL. Between this level and the higher exciton origin of the special pair there are many one- and two-quantum vibrational satellites of the three lower exciton states (all forbidden for Δ=0), corresponding to b=8-65 (see Table S3). Thus, the upper exciton origin (fourth ZPL) should be labeled as 66^{P1P2}.

In the presence of coupling the sequence of ZPLs is 1^{Chl}, 2^{Phe}, 6^{P1P2}, and 90^{P1P2} (see Table S3).Vibrational satellites of the lowest 1^{Chl} state are in quasi-resonance with the 2^{Phe} and 6^{P1P2} ZPLs. First of all, this changes the participation of the pigments in these levels. Both 2^{Phe} and 6^{P1P2} now contain a significant contribution of Chl_{D1} (in contrast to the non-resonant cases, when the 2^{Phe} and 6^{P1P2} states are predominantly localized at Phe $_{D1}$ and P_{D1}/P_{D2}, respectively) (compare Tables S1-S3). Secondly, the resonant vibrational sublevels borrow significant part of the dipole strength from ZPLs. This produces the vibronic manifold ($\{b^1\}=3^{1z}, 4^1, 5^{1m}, 7^{1z}$) with very intense 3^{1z} and 7^{1z} pseudo-ZPLs localized mostly at Chl_{D1} (with admixture of Phe $_{D1}$).

At higher energies there are one-quantum sublevels of the 2^{Phe} and 6^{P1P2} states ($\{b^2\}=8^2, 9^2, 10^{2m}, 11^2$ and $\{b^6\}=18^6, 19^6, 20^6, 21^{6m}$) superimposed with two-quantum sublevels of the 1^{Chl} ZPL (see inset in Figure 4). The higher exciton origin 90^{P1P2} is mixed with a large number of high-order quasi-degenerate vibrational satellites from lower exciton states, producing a group of states (b=83-100) with the same total dipole strength as the 66^{P1P2} free exciton origin (see second inset in Figure 4 and parameters of these states listed in Table S3).

Exciton-vibrational coherences, 2D oscillating peaks.

Now we switch to study the coherences between the vibronic states as they appear in the 2D-echo experiment. As an example we analyze the oscillating components in the stimulated emission (SE) part of the rephasing 2D response, corresponding to coupling to a single vibrational mode with Ω=340 cm^{-1} in the absence of disorder. Positions and amplitudes of the oscillating SE components as a function of excitation and emission frequency are shown in Figure 5. Other parameters of these components, such as oscillating frequency and degree of exciton mixing between the involved sites P_{nm} (see Methods) are listed in Table S4 (see ESI†). To avoid confusion with the numbering of vibronic states we will label the sites n,m by letters A, B, C, and D (that stand for P_{D1}, P_{D2}, Chl_{D1}, and Phe_{D1}, respectively).

As we have seen, coupling of the set of electronic states to just one vibrational mode yields a complicated manifold of vibronic states due to mixing between the sites. Coherent excitation of this whole vibronic manifold in a 2D-echo experiment produces an even more complex variety of coherences, involving different pairs of vibronic states. Analysis of the most intense SE components allows to identify 7 different types of coherence (they are shown by different colors in Figure 5 and are included as separate groups in Table S4).

1. Pure excitonic coherence between the true ZPLs. This type of coherence occurs between the excitonic origins (true ZPLs), that is between the 1^{Chl}, 2^{Phe}, 3^{P1P2}, and 4^{P1P2} states (in Figure 5 and Table S4 we drop the superscripts and label them as 1, 2, 3, and 4). The most intense are the 1-3, 1-2, and 1-4 components, with oscillating frequencies Ω_{osc} in the 100-150 cm^{-1} region and around 300 cm^{-1}. Notice that we do not consider low-frequency (<50 cm^{-1}) components, so the 2-3 coherence is not considered here. For the most intense excitonic coherence 1-3 we obtain a high degree of mixing between the special pair and Chl_{D1} (P_{AC},P_{BC}>0.45). The 1-2 coherence is determined mostly by Chl_{D1}-Phe_{D1} mixing (P_{CD}>0.6). The 1-4 coherence contains a mixing of the same pigments as in the 1-3 coherence, but the degree of mixing is not as high (P_{AC},P_{BC}=0.27-0.29) because level 4 is only weakly allowed. The excitonic coherences typically give rise to two symmetric SE peaks below and above the diagonal in the $\{\omega_\tau, \omega_t\}$ plane (symmetric duplet). But there may be additional, minor SE peaks associated with the same coherence. Thus, emission to higher vibrational sublevels of the ground state produces additional two (or four) weak components at lower ω_t. For example, the two main 1-3 peaks correspond to emission to the lowest c=1 sublevel of the ground state (see Table S4). In addition, there is also emission to the next ground-state sublevel (actually, to one of the four-fold degenerate sublevels c=2-5), producing an additional pair of weak 1-3 components (see Figure 5).

2. Excitonic coherence between the true ZPL and pseudo-ZPL. This type of coherence occurs between the exciton origin ('true' ZPL) and a vibrational sublevel, borrowing significant part of dipole strength due to resonance with another ZPL. Coherence between true ZPL and such a pseudo-ZPL looks like a pure excitonic coherence, displaying a high degree of exciton mixing, and producing a symmetric duplet on a 2DFT map. In our example (Ω=340 cm^{-1}) the component of this type is the 3-17^{4z} coherence, characterized by high degree of P_{D1}-P_{D2} mixing with P_{AB}=0.71. The intensity of the 3-17^{4z} duplet is not high because 17^{4z} borrows dipole strength from the relatively weak highest exciton component. Notice, however, that in the case of low-frequency resonance (Ω=120 cm^{-1}) there are more intense pseudo-ZPLs (3^{1z} and 7^{1z}) due to resonance with intense lower exciton origins. In this case the intensities of the SE peaks due to coherences with pseudo-ZPLs are comparable with the true exciton peaks (see Table S5).

3. Coherence between two 'magic' vibronic levels. We have seen that the 4 vibrational satellites of each excitonic origin contain one that corresponds to the 'magic' direction, that is the direction of correlated nuclear motion. This 'magic' level is shifted exactly by Ω from the excitonic origin and has exactly the same participation of the pigments as the ZPL origin. Coherence between two 'magic' sublevels of different exciton states is characterized by the same oscillating frequency and the same values of exciton mixing P_{nm} as the coherence between the corresponding ZPLs. In our example the most pronounced is the coherence between the magic sublevels of the 1 and 3 origins, that is the 5^{1m}-14^{3m} coherence. The corresponding Ω_{osc} and P_{nm} values are the same as for the pure exciton 1-3 coherence (within the accuracy of numerical modeling) as shown in Table S4. In the 2DFT map the 5^{1m}-14^{3m} coherence contributes an asymmetric (shifted below the diagonal) duplet due to emission to the *c*=5 sublevel of the ground state.

4. Mixed coherence between a ZPL and the vibrational sublevel of another state. Coherence between an excitonic origin and a vibrational satellite of another exciton state contains some exciton mixing, but to a lesser extent as compared to the coherence between ZPLs of the same states. For example, the 3-8^1 coherence (between 3^{P1P2} ZPL and vibrational satellite of the 1^{Chl} state) is 'less excitonic' (with P_{AC}=0.29, P_{BC}=0.35) than the pure excitonic 3-1 coherence (with P_{AC}=0.45, P_{BC}=0.46). The 1-13^3 coherence (between the 1^{Chl} ZPL and the satellite of the 3^{P1P2} state) is even less excitonic (with P_{AC}=0.13, P_{BC}=0.14). On the 2DFT map these mixed coherences still seem 'excitonic': they produce symmetric duplets. The oscillating frequency equals to the exciton splitting plus (or minus) the vibrational frequency (with an accuracy given by the splitting within the 4 vibrational sublevels).

5. Mixed coherence between a ZPL and its own vibrational sublevel. Coherence between a ZPL and a vibrational satellite of the same state (for example, 1-8^1 or 3-13^3 coherence) can contain some exciton mixing if participation of the pigments in the vibrational sublevel is different from that of the ZPL. This difference is significant for the 1 and 8^1 states (see Table S2). As a result, the 1-8^1 coherence is different from purely vibrational, containing exciton mixing (that is not as pronounced as in the 3-8^1 coherence, but still sizable). On a 2DFT map this coherence produces a symmetric duplet. The 3-13^3 coherence is closer to purely vibrational, giving an almost symmetric quadruplet. But the degree of exciton mixing in the 3-13^3 coherence is still sizable (although lower than in 1-13^3 coherence). Therefore, we can classify the coherences of this type as mixed exciton-vibrational (vibronic). It is worth noticing that the oscillating frequencies for such coherences are close to the vibrational frequency Ω (see Table S4).

6. Vibrational coherence between a ZPL and its own 'magic' sublevel. Coherence between a ZPL and the 'magic' vibrational sublevel of the same exciton state produces a purely vibrational coherence without any appreciable exciton mixing. The SE peaks have the form of a symmetric vibrational quadruplet, oscillating at frequency Ω. Most intense are 1-5^{1m} and 3-14^{3m} quadruplets.

7. Vibrational coherence between a ZPL and the 'magic' sublevel of another state. Coherence between a ZPL and the 'magic' vibrational sublevel of some other exciton state also produces purely vibrational coherence without exciton mixing. The SE peaks have the form of a deformed quadruplet. Most intense are the 3-5^{1m} and 1-14^{3m} quadruplets. The oscillating frequency equals to the exciton splitting plus (or minus) Ω.

Explanation of the 2D frequency maps of the PSII-RC.

Next we have modeled the 2DFT maps (see Methods) corresponding to the oscillating frequencies of Ω_{osc}=120, 340, and 740 cm^{-1}. The calculated maps are compared to the measured ones in Figure 6. Note that each of these maps originates from many different oscillatory contributions.

The 120 cm^{-1} map contains a single peak below the diagonal, determined mostly by the excitonic coherences involving three lower exciton ZPLs as well as pseudo-ZPLs appearing in the case of coupling to a quasi-resonant 120 cm^{-1} vibrational mode. Coupling to the 120 cm^{-1} mode also gives rise to (i) mixed excitonic-vibrational coherences producing the SE peaks oscillating with a frequency near 120 cm^{-1}, and (ii) pure vibrational coherences in the SE oscillating exactly at 120 cm^{-1}, as well as (iii) vibrational coherences in the ground-state bleach (GSB) oscillating at 120 cm^{-1}. But these vibrational and mixed coherences (involving relatively weak vibrational satellites) produce the 2DFT components whose intensities are much lower than the components determined by the excitonic coherences (occurring between intense ZPLs separated by energy gaps near 120 cm^{-1}). As a result the total degree of exciton mixing P_{coh} (see Methods) for the off-diagonal peak is very high (P_{coh}=0.73). Therefore, we conclude that the coherence observed in the 120 cm^{-1} map can be classified as predominantly excitonic.

The 340 cm^{-1} map contains contributions from the mixed exciton-vibrational (vibronic) coherences (together with contributions from pure vibrational coherences both in the SE and GSB). The configuration of this map resembles a pure vibrational map (because the mixed coherence gives almost the same symmetric SE quadruplet on the 2DFT map as the pure vibrational coherence). The total weighted degree of exciton mixing P_{coh} is maximal for the diagonal peak of the quadruplet and equals to P_{coh}=0.31. The contributions from excitonic coherences also appear when the (disorder-dependent) gap between the higher exciton level and any of the lower ones is equal to 340 cm^{-1}. Additonal excitonic coherences near 340 cm^{-1} can emerge from the mixing of the excitonic transitions with a quasi- resonant vibrational mode (265 or 340 cm^{-1} mode), giving a pseudo-ZPL separated from the lower ZPLs by about 340 cm^{-1} (depending on the realization of the disorder). Both these excitonic coherences contribute to the off-diagonal $\{\omega_\tau, \omega_t\}=\{\Omega_{osc}, 0\}$ peak (counting from the energy of the main electronic transition, corresponding to the 680 nm band in the experiment). But the intensities of these components are relatively weak due to the small dipole strength of the higher excitonic level. The resulting degree of the weighted exciton mixing for this peak (encircled in Figure 6) is not so high, P_{coh}=0.28, which is comparable with P_{coh}=0.31 for the diagonal peak determined by vibronic (exciton-vibrational) coherences. Thus, the 340 cm^{-1} map contains two types of coherence: predominantly excitonic and vibronic (with a significant degree of exciton mixing).

The 740 cm^{-1} oscillating frequency is far from the exciton resonances. Therefore, no significant excitonic contributions are expected. Indeed, the off-diagonal 'excitonic' peak has no significant exciton mixing (P_{coh}=0.07) in contrast with the 340 cm^{-1} case (P_{coh}=0.28). The degree of exciton mixing is maximal for the diagonal peak of the vibronic quadruplet and equals to P_{coh}=0.19. This is lower than the P_{coh}=0.31 value for a similar vibronic peak in the 340 cm^{-1} map. We conclude that the 740 cm^{-1} map is largely determined by vibronic coherence (with a low degree of exciton mixing) and a pure vibrational one.

Comparing the two high-frequency 2DFT maps (that is 340 and 740 cm^{-1} maps consisting of separated peaks) we conclude that when the vibrational frequency approaches the largest exciton splitting in the PSII-RC this results in: (i) an increase of excitonic mixing P_{coh} in the diagonal peak determined by vibronic coherences; (ii) an increase in the amplitude of the off-diagonal $\{\omega_\tau, \omega_t\}=\{\Omega_{osc}, 0\}$ peak due to pure excitonic coherences (as shown in Figure 6); and (iii) an increase of the weighted degree of excitonic mixing P_{coh} for this off-diagonal peak.

Based on our numerical examples it can be concluded that the 4-state model of PSII-RC explored here, allows a better explanation of the 2DFT maps as compared to the previous 2-state model.[12] In particular, our model gives a better fit of the excitonic and vibronic peaks in the 340 cm^{-1} map. Importantly, the 4-state model is capable (in contrast with the 2-state model) to reproduce the excitonic 120 cm^{-1} map.

3. Discussion

We have seen that the mixing of excitonic transitions coupled to vibrations produces a complicated manifold of excitonic-vibrational (vibronic) eigenstates. Most interesting is the case when some vibrational modes are in quasi-resonance with the exciton splitting. This can be expected for most of the photosynthetic light-harvesting and RC complexes that typically are characterized by a rich spectrum of vibrational modes together with a large spread of exciton splittings due to a combination of many interacting pigments and spectral disorder. For some complexes it may not be the case. For example, in bacterial RC the frequency of most intense 130 cm^{-1} vibration is much less than the exciton splitting and the gap between the exciton and primary CT state.[26] As a result, the charge transfer dynamics contains predominantly vibrational coherences.[26] In that case a charge separation scheme can be build with neglecting the mixing effects.[27]

In contrast, in the PSII-RC there are exciton splittings that are in resonance with the intense 120 and 340 cm^{-1} vibrations. Resonance exciton-vibrational mixing can dramatically change the vibronic manifold around the spectral region where such a mixing occurs. In principle, this phenomenon can affect both the rate and the direction of energy transfer. Moreover, the mixing with vibrations can also affect the charge separation dynamics if the vibrational frequency is close to the energy gap between the excited primary donor and the first CT state.

Resonant vibrations and energy transfer.

In our numerical examples we have shown that coupling the PSII-RC excitonic manifold to resonant vibrations can (i) change the character of delocalization of the excited states, and (ii) produce additional vibronic pseudo-ZPLs borrowing a significant part of the dipole strength from the pure excitonic origins (ZPLs). Both these phenomena can promote an effective energy transfer with subsequent charge separation via some specific pathway. For example, the 340 cm^{-1} mode (resonant with the exciton splitting within the special pair) breaks the symmetry within the special pair, producing an additional pseudo-ZPL level localized at P_{D1}. Thus, the 340 cm^{-1} mode can affect the exciton relaxation within the special pair and subsequently lead to charge separation via $P_{D2}^{+}P_{D1}^{-}$. Another example is the 120 cm^{-1} mode that is in quasi-resonance with the gap between the lowest exciton levels (1^{Chl}-2^{Phe} and 1^{Chl}-6^{P1P2}). First, this exciton-vibrational resonance changes the delocalization of the 2^{Phe} and 6^{P1P2} ZPLs. These states (initially mainly localized at Phe_{D1} and P_{D1}/P_{D2}, respectively) become more delocalized due to the admixture of Chl_{D1}. Secondly, this resonance produces an additional pseudo-ZPL state localized at Chl_{D1} (with admixture of Phe_{D1}). Thus, the 120 cm^{-1} mode can promote another charge separation pathway via $Chl_{D1}^{+}Phe_{D1}^{-}$.

Resonant vibrations and charge separation.

In Figure 7a we show the energies of the ZPLs of the four exciton states (as they appear in the present 4-state model, that is 0, 116, 143, and 436 cm^{-1} counting from the lowest ZPL), the energy of the primary charge-transfer $P_{D2}^{+}P_{D1}^{-}$ state (–261 cm^{-1} after its mixing with the excited states[4]), and energies of the localized (non-mixed) CT states $Chl_{D1}^{+}Phe_{D1}^{-}$, $P_{D1}^{+}Chl_{D1}^{-}$, and $P_{D1}^{+}Phe_{D1}^{-}$ (–317, –466, and –716 cm^{-1}, respectively[25]). It is remarkable that the 340 cm^{-1} mode is in quasi-resonance not only with the splitting within the special pair, but also with the energy gaps between the primary donors and the first CTs in the two charge separation pathways (that is $Chl_{D1} \rightarrow Chl_{D1}^{+}Phe_{D1}^{-}$ and $P_{D1}P_{D2} \rightarrow P_{D2}^{+}P_{D1}^{-}$ transfers with the gaps of 317 and 377 cm^{-1}, respectively). When the exact splitting value (determined by the disorder) is out of resonance, the vibronic wavefunctions of the excited and CT state are only weakly overlapping (as shown in Figure 7b). In the resonant case the vibrational sublevels of the two states are strongly mixed, producing vibronic wavefunctions that are delocalized between the electronic states involved (Figure 7c).

The influence of the vibronic overlap on the charge transfer dynamics is illustrated in Figure 7d and 7e. Here we have calculated the dynamics of the excited-state vibrational wavepacket created by impulsive excitation of the mixed exciton-CT configurations shown in Figures 7b and 7c, respectively. The relaxation dynamics of the initially created wavepacket is calculated using the Redfield theory in the exciton-vibrational basis, as described in detail in ref. 26. Initially the wavepacket is localized in the Condon region corresponding to the left side of the excited state potential surface (around $x=-2$). Then the wavepacket exhibits coherent motion within the excited-state potential well (with a period of about 100 fs corresponding to the 340 cm^{-1} vibration). Penetration of some part of the wavepacket into the CT region produces coherent oscillatory motion also within the CT potential. Finally, the excitation density is localized near the bottom of the CT state. The transfer to the CT state is most effective in the resonant case (Figure 7e), when the vibronic wavefunctions are strongly overlapping (Figure 7c). A slight change in the energy gap (from 340 to 320 cm^{-1}) gives significantly (about 2-times) slower transfer (Figure 7d) due to a decrease in the wavefunction overlap (as shown in Figure 7b). Further detuning of the gap (from 340 to 300 cm^{-1}) results in 4-times slower transfer (data not shown).

The example shown in Figure 7 demonstrates how important is the exciton-vibrational resonant mixing in order to obtain an effective charge transfer. In principle, a similar resonance effect also occurs for the energy transfer channels, but in this case the difference in rates is not so pronounced (because of the smaller relative displacement of the diabatic states, that produces a good vibrational overlap even in the off-resonant case).

According to Figure 7, the 120 cm^{-1} mode connects the two charge separation pathways, while the charge separation via $P_{D2}^{+}P_{D1}^{-}$ can be additionally speed up by the 190 and 265 cm^{-1} modes (present in the 2D experimental data[6] and quasi-resonant with the gaps between the CT states in this pathway). Also the direct formation of the $P_{D2}^{+}P_{D1}^{-}$ and $P_{D1}^{+}Chl_{D1}^{-}$ states from the higher and lower exciton levels of the special pair can be promoted by the vibrations with frequencies close to the gaps of 697 and 582 cm^{-1}, respectively (notice that these frequencies appear with significant amplitude in the 2D experimental data[6]).

Coherent phenomena upon different excitation conditions.

The most straightforward way to study coherent phenomena in photosynthesis is connected with broad-band excitation of the antenna complexes or the RC by a short laser pulse. Such excitation creates a coherent superposition of the exciton (or exciton-vibrational) eigenstates with subsequent evolution of these quantum coherences that are observed as oscillations in the nonlinear responses (like pump-probe or 2D-echo signals). Study of these oscillatory features gives important information about the properties of the eigenstates, about the physical origins and pathways of energy/electron transfers.[28-32]

In a series of papers[13,17,21,26,33] it was pointed out that a (dynamic) coherence between eigenstates is possible also under non-coherent excitation. Even if only populations of eigenstates are created initially, the coherences between them (accompanied by sizable oscillations) still can be created due to non-secular transfers, i.e. transfers from populations to coherences. It was first demonstrated for the two-state model coupled to one vibration,[33] and later it was confirmed in modeling of the coherent electron transfer dynamics in the bacterial RC.[26] In both cases it was possible to explain the effect of the formation of coherent oscillatory dynamics within the limits of Redfield theory with the full relaxation tensor in the basis of exciton-vibrational eigenstates. In more advanced (nonperturbative) theories, the coherence upon non-coherent excitation may appear due to strong coupling to the bath.[13,17] Notice, however, that in all these examples the coherent effects appear after non-coherent, but still impulsive excitation. For example, the coherent dynamics emerging from the initial population of any eigenstate can be observed only if this population is created on a time scale, faster than the oscillating period of the coherence. Therefore, in natural conditions, where the excitation is non-coherent and non-impulsive, the effects of dynamic coherence cannot be observed.[34] The only factor, that can contribute to the effectiveness of natural photosynthesis is the inner coherence, i.e. a coherent mixing of the electronic or/and vibrational wavefunctions within eigenstates. Recently a modeling of the steady-state limit of energy transfer in antenna has been performed with highlighting of the role of such coherences.[35]

4. Methods

Reduced model of PSII-RC.

The full exciton model of PSII-RC considers the excited states of the 8 pigments (6 chlorophylls (Chl) and 2 pheophytins (Phe)) coupled to several (at least 4) charge-transfer (CT) states.[4,6,25,36-41] The explicit modeling of exciton-vibrational dynamics for such a 12-state model is too complicated numerically (even in the simplest case of coupling to just one vibrational mode an exact model must include 12 nuclear coordinates for each of the 12 electronic diabatic states). In principle, the model can be reduced to a smaller number of states. For example, the phenomena of exciton mixing and coherent energy/electron transfers occur within a cluster containing 6 strongly coupled core pigments (4 Chl's and 2 Phe's) mixed with one (primary) CT state.[4,6] Thus, in the modeling of coherent exciton-vibrational dynamics we can restrict ourselves to the 7-state model. However, also for this model an exact solution of the exciton-vibrational problem is still too complicated.

In the present modeling we use a 4-state model that includes the pigments from the active branch of the PSII-RC: P_{D1}, P_{D2}, Chl_{D1}, and Phe_{D1}. The pigment-pigment couplings and the transition dipoles are the same as those in our previous modeling.[4,6,25] The coupling to vibrations is described in the basis of exciton-vibrational eigenstates (as discussed below). This allows an explicit treatment of the coherent exciton-vibrational dynamics, but only for a limited number of vibrational modes. Thus, we cannot use a realistic spectral density, like we did in previous modeling based on a Redfield approach in the pure exciton basis.[4,6,25] In the present modeling we include the coupling of the relevant electronic states to just a single mode. In particular, this means that we cannot account for the reorganization shifts emerging from the coupling to all the vibrations and phonons. Consequently, the site energies used in present modeling should be red-shifted to compensate for the absence of the reorganization shift. In our numerical examples the unperturbed energies of the zero-phonon transitions of the four sites {P_{D1}, P_{D2}, Chl_{D1}, Phe_{D1}} are {15020, 15020, 14780, 14860} cm^{-1}. These values give the same exciton splittings as in previous models (as can be seen by comparing Figure 1 of this paper and Figure 4 from ref. 4).

The disorder is described by uncorrelated random shifts of the site energies taken from a Gaussian distribution with a width of σ (full width at half maximum, FWHM). We remind that the apparent disorder of the zero-phonon energies in the Redfield picture is given by the combined action of the energetic disorder (site inhomogeneity) and the disorder of reorganization shifts in the exciton representation. To compensate for the absence of the full reorganization-induced disorder, we increase the energetic disorder from $\sigma=95\ cm^{-1}$ (used in the Redfield picture) to $\sigma=180\ cm^{-1}$ in the present modeling (the value adjusted from the fit of 2DFT maps).

Exciton-vibrational Hamiltonian.

The system (exciton-vibrational) Hamiltonian in the site (diabatic) representation is:

$$\begin{aligned}
H_{ex-vib} &= H_g + H_e + H_f \\
H_g &= |g\rangle \left[\sum_{j,s} \tfrac{1}{2}\Omega_j (\Delta_g^{js})^2 + \sum_{j,s} \Omega_j (\beta_{js}^{+}\beta_{js} + \tfrac{1}{2}) - \sum_{j,s} \tfrac{1}{\sqrt{2}} \Omega_j \Delta_g^{js} (\beta_{js} + \beta_{js}^{+}) \right] \langle g| \\
H_e &= \sum_n |n\rangle \left[\omega_{n0} + \sum_{j,s} \tfrac{1}{2}\Omega_j (\Delta_n^{js})^2 + \sum_{j,s} \Omega_j (\beta_{js}^{+}\beta_{js} + \tfrac{1}{2}) - \sum_{j,s} \tfrac{1}{\sqrt{2}} \Omega_j \Delta_n^{js} (\beta_{js} + \beta_{js}^{+}) \right] \langle n| + \\
&\quad + \sum_{nm} |n\rangle M_{nm} \langle m| \\
H_f &= \sum_{nm} |nm\rangle \left[\omega_{n0} + \omega_{m0} + \sum_{j,s} \tfrac{1}{2}\Omega_j (\Delta_{nm}^{js})^2 + \sum_{j,s} \Omega_j (\beta_{js}^{+}\beta_{js} + \tfrac{1}{2}) - \sum_{j,s} \tfrac{1}{\sqrt{2}} \Omega_j \Delta_{nm}^{js} (\beta_{js} + \beta_{js}^{+}) \right] \langle nm| + \\
&\quad + \sum_{nn'mm'} |nm\rangle \left[\delta_{nn'} M_{mm'} + \delta_{nm'} M_{mn'} + \delta_{mn'} M_{nm'} + \delta_{mm'} M_{nn'} \right] \langle n'm'|
\end{aligned} \tag{1}$$

The basic states are given by a direct product of the electronic wavefunctions (ground $|g\rangle$, one-exciton $|n\rangle$, and two-exciton $|nm\rangle$) and vibrational wavefunctions $|a_{js}\rangle$ for the j-th mode depending on the effective nuclear coordinates (labelled 's'). The basis vibrational wavefunctions $|a_{js}\rangle$ are unshifted, that is they have zero displacement along the s-coordinates. The creation and annihilation phonon operators β_{js}^{+} and β_{js} for j-th nuclear mode work in this unshifted basis. Displacements of the electronic surfaces along the s-coordinates (Δ_g^{js}, Δ_n^{js}, Δ_{nm}^{js}) are accounted for by the shifting operators $\Omega_j\Delta^{js}(\beta_{js}+\beta_{js}^{+})/\sqrt{2}$, where Ω_j is the frequency of the j-th mode. Electronic excitations in the site representation correspond to the g→n and n→nm transitions with the electronic transition dipoles $\mathbf{d}_n$, $\mathbf{d}_{nm,n}=\mathbf{d}_m$ and zero-phonon transition energies ω_{n0}, $\omega_{nm,n}=\omega_{m0}$. The interaction between the diabatic states is given by the energies M_{nm} that are supposed to be independent of the vibrational coordinates. Diagonalization of the Hamiltonian (1) gives the exciton-vibrational (vibronic) eigenstates:

$$\begin{aligned}
&H_g C^g = C^g E^g; \quad |c\rangle = \sum_a C_{ac}^g |g, a\rangle; \quad E_{cc'}^g = \delta_{cc'}\omega_c \\
&H_e C^e = C^e E^e; \quad |b\rangle = \sum_{n,a} C_{n,ab}^e |n, a\rangle; \quad E_{bb'}^e = \delta_{bb'}\omega_b \\
&H_f C^f = C^f E^f; \quad |r\rangle = \sum_{nm,a} C_{nm,ar}^f |nm, a\rangle; \quad E_{rr'}^f = \delta_{rr'}\omega_r
\end{aligned} \tag{2}$$

where $|g,a\rangle$, $|n,a\rangle$, and $|nm,a\rangle$ denote a product of the electronic $|g\rangle$, $|n\rangle$, and $|nm\rangle$ and vibrational wavefunctions $|a\rangle$, where $|a\rangle=|a_{11}, \ldots a_{js},\ldots\rangle$ is the product of wavefunctions corresponding to the s-th coordinate of the j-th vibrational mode,. The C^g, C^e, and C^f are the matrices, whose elements show participation of the unshifted states $|g,a\rangle$, $|n,a\rangle$, and $|nm,a\rangle$ in the vibronic states of the ground *c*, one-exciton *b*, and two-exciton manifold *r*. Transition dipoles between the ground, one- and two-exciton vibronic states are:

$$\begin{aligned} \mathbf{d}_{bc} &= \sum_{n,a} C^{e}_{n,ab}\,\mathbf{d}_{n}\,C^{g}_{ac} \\ \mathbf{d}_{rb} &= \sum_{n,m,nm,a} C^{f}_{nm,ar}\,(\mathbf{d}_{m}\,C^{e}_{n,ab}+\mathbf{d}_{n}\,C^{e}_{m.ab}) \end{aligned} \qquad (3)$$

Nuclear coordinates for the 4-state model.

In principle, the Hamiltonian (1) with a given number of diabatic electronic states allows to build different models depending on the choice of the effective nuclear (vibrational) coordinates. The simplest model implies just a single nuclear coordinate (i.e. the same for all the states), whereas electronic states can be characterized by different displacements along this coordinate. Such a model describes in some simplified manner the vibrational wings of the absorption profile, and coupled exciton-vibrational dynamics within the excited-state manifold (including coherent dynamics). In fact, the vibrations coupled to different electronic states are generally independent, so in a more realistic description each diabatic state should be characterized by its own vibrational coordinate for each vibrational mode. For example, a dimer, containing two molecules coupled to a single intra-molecular vibration, should be described by an effective two-dimensional nuclear space (**x**,**y**). If the ground-state potential has its minimum at (0,0), then the excited-state potentials of the 1st and 2nd diabatic states (displaced along **x** and **y** by Δ) have their minimums at (Δ,0) and (0, Δ). The two-exciton state (with both diabatic states excited) has its minimum at (Δ, Δ). Exciton mixing of these potentials produces two delocalized states with the potential minima between the diabatic minima at ($\Delta/2$, $\Delta/2$) in the strong coupling limit, or two localized states with minima near the unperturbed values of (Δ,0) and (0, Δ) in the weak coupling limit. (Obviously, such a difference does not exist in a one-dimensional model with the two molecules having the same displacement Δ along a single coordinate. The exciton states in this case will be displaced by Δ both in strong and weak coupling limits!).

Notice that the model of a dimer with the two nuclear coordinates (as described above) was first considered by Förster,[42] who demonstrated that the energy transfer rate in a weak coupling limit is given by the square of interaction energy between the two states and by the overlap of the vibrational wavefunctions. Supposing that the nuclear degrees of freedom are equilibrated it is possible to obtain a compact expression for the rate of energy transfer between the two localized states (Förster formula[42]). In a more general case of arbitrary strong coupling, the vibrational sub-levels of the two electronic states become mixed, thus producing exciton-vibrational (vibronic) states delocalized over the two electronic states.[11,18,43] The dynamics of the excited states becomes more complicated containing an interplay between the excitonic and vibrational coherences. This dynamics can be described using the Redfield theory in the basis of delocalized vibronic states,[26,33,44-46] or more sophisticated (nonperturbative) approaches.[47,48]

In this paper we explore the exciton-vibrational coherences in a model containing 4 electronically excited states coupled to a single vibrational mode with the frequency Ω. Each of the four diabatic states (n=1, 2, 3, 4) is shifted along its own effective nuclear coordinate, reflecting a coupling to its own intra-molecular vibration. Therefore, we need 4 nuclear coordinates x_s (s=1-4) reflecting the coupling of this mode to the states n=1-4. Similar to the case of a dimer, the displacements of the electronic states along the four coordinates in 4-dimensional space (i.e. Δ_g^s, Δ_n^s, Δ_{nm}^s, where s=1-4) are:

$\{\Delta_g^1,\Delta_g^2,\Delta_g^3,\Delta_g^4\}=\{0,0,0,0\}$ for the ground state $|g\rangle$;
$\{\Delta_n^1,\Delta_n^2,\Delta_n^3,\Delta_n^4\}=\{\Delta,0,0,0\}$ for the excited state $|n\rangle=|1\rangle$;
$\{\Delta_n^1,\Delta_n^2,\Delta_n^3,\Delta_n^4\}=\{0,\Delta,0,0\}$ for the excited state $|n\rangle=|2\rangle$;
……………………………………………………………….
$\{\Delta_{nm}^1,\Delta_{nm}^2,\Delta_{nm}^3,\Delta_{nm}^4\}=\{\Delta,\Delta,0,0\}$ for the two-exciton state $|nm\rangle=|1,2\rangle$;

$\{\Delta_{nm}^1,\Delta_{nm}^2,\Delta_{nm}^3,\Delta_{nm}^4\}=\{\Delta,0,\Delta,0\}$ for the two-exciton state $|nm\rangle=|1,3\rangle$;
……………………………………………………………………….

where we suppose that the displacement Δ of the n-th excited state with respect to the ground is the same for all the states. The displacement of the ground state can be chosen as $\{0,0,\ldots 0\}$, or, alternatively, $-1/2\{\Delta,\Delta,\Delta,\Delta\}$. In this alternative configuration the displacements of the diabatic states with respect to the basis (unshifted) ones are two times smaller, i.e.

$\{\Delta_g^1,\Delta_g^2,\Delta_g^3,\Delta_g^4\}=1/2\{-\Delta,-\Delta,-\Delta,-\Delta\}$ for the ground state $|g\rangle$;
$\{\Delta_n^1,\Delta_n^2,\Delta_n^3,\Delta_n^4\}=1/2\{+\Delta,-\Delta,-\Delta,-\Delta\}$ for the excited state $|n\rangle=|1\rangle$;
$\{\Delta_n^1,\Delta_n^2,\Delta_n^3,\Delta_n^4\}=1/2\{-\Delta,+\Delta,-\Delta,-\Delta\}$ for the excited state $|n\rangle=|2\rangle$;
……………………………………………………………….
$\{\Delta_{nm}^1,\Delta_{nm}^2,\Delta_{nm}^3,\Delta_{nm}^4\}=1/2\{+\Delta,+\Delta,-\Delta,-\Delta\}$ for the two-exciton state $|nm\rangle=|1,2\rangle$;
$\{\Delta_{nm}^1,\Delta_{nm}^2,\Delta_{nm}^3,\Delta_{nm}^4\}=1/2\{+\Delta,-\Delta,+\Delta,-\Delta\}$ for the two-exciton state $|nm\rangle=|1,3\rangle$;
……………………………………………………………………….

The wavefunctions for the ground, one- and two-exciton eigenstates can be calculated in the basis of the unshifted wavefunctions $|a\rangle=|a_1,a_2,a_3,a_4\rangle$. Each of the numbers a_1–a_4 run integer values from 0 to $(\nu-1)$, where ν is the number of the basis wavefunctions per each coordinate x_s (in our numerical examples $\nu=6$).

Diagonalization of Hamiltonian (1) with zero displacements ($\Delta=0$) gives the zero-phonon lines (ZPL) with the same energies and dipole strengths as the exciton transitions in the pure exciton picture. Each ZPL is accompanied by vibrational satellites, including a 4-times degenerate sublevel (responsible for transitions involving one vibrational quantum), a 10-fold degenerate (two-quantum) sublevel, etc. For $\Delta=0$ the dipole strength of all these sublevels equals to zero.

For nonzero displacements the exciton and vibrational sublevels are mixed, producing a complex manifold of vibronic eigenstates. If the displacements are small ($\Delta^2/2 \ll 1$) we still can distinguish between the ZPLs and their vibrational satellites. Due to mixing of the displaced states, the vibrational satellites borrow dipole strength from the ZPL origins (proportional to Δ^2) and become non-degenerate. The borrowing of dipole strength is essentially non-uniform, that is participation of the pigments in each of the vibrational sublevels is different from their participation in the ZPL origin. In the $\Delta^2/2 \ll 1$ case this difference is not large (thus allowing an assignment of the satellite to a particular ZPL). But if a vibrational mode is in resonance with the exciton splitting, the properties of both the ZPLs and quasi-resonance vibrational sublevels can be disturbed dramatically (even in the case of $\Delta^2/2 \ll 1$).

There is, however, one vibrational wavefunction (that is one of the four one-quantum satellites), that is not affected by the non-uniform mixing. This wavefunction is oriented along the ‘magic’ direction, corresponding to a correlated nuclear motion within all the four sites. The ‘correlated’ direction is given by the $\mathbf{x}_1+\mathbf{x}_2+\mathbf{x}_3+\mathbf{x}_4$ vector in 4-dimensional nuclear space. The corresponding vibrational state is higher in energy than its ZPL by exactly Ω. The participation of the pigments in this state is exactly the same as in the ZPL. The coherence between the ZPL and the ‘magic’ level corresponds to a pure vibrational motion without any beats between the participating pigments (because the motion along $\mathbf{x}_1+\mathbf{x}_2+\mathbf{x}_3+\mathbf{x}_4$ does not change the degree of mixing between the four sites). In other words, the ‘correlated‘ direction is the direction of no-energy-transfer. The other three one-quantum wavefunctions contain some anti-correlated part (dependence on $\mathbf{x}_n-\mathbf{x}_m$). Different $\mathbf{x}_n-\mathbf{x}_m$ values correspond to different degrees of mixing between the sites *n* and *m*. For this reason a coherent motion along the $\mathbf{x}_n-\mathbf{x}_m$ direction (initiated by a coherent excitation of such a non-correlated wavefunction and its ZPL) will produce sizable quantum beats between the sites *n* and *m*. Non-coherent equilibration of this motion corresponds to energy transfer between the two sites. If the reorganization energy ($\Omega\Delta^2/2$) exceeds the exciton coupling M_{nm} between these sites, then the equilibration will lead to a dynamic localization of the excitation on *n* or *m*.

Exciton-vibrational structure of the ground-state absorption (OD).

We calculate the exciton-vibrational structure of the OD supposing the coupling to a single vibrational mode. In the examples shown in Figures 2-4 we do not consider the effect of the disorder, we use the unperturbed values of the site energies. The components of the stick spectra in Figures 2-4 correspond to the $c \to b$ transitions. Intensity of each transition is given by the square of the dipole moment (3), and the energy is $\omega=\omega_b-\omega_c$. Calculation is restricted to the low-temperature limit, when transitions occur only from the lowest vibrational level of the ground state, that is c=1. In this case the absorption components can be characterized by a single index b corresponding to the number of the one-exciton vibronic state (the vibronic states are numbered in increasing order of their energies).

Degree of exciton mixing in the 2D oscillations.

In Figure 5 we analyze the oscillating components in the stimulated emission (SE) part of the rephasing 2D response. The 2D-echo response is calculated for a parallel polarization of the four pulses (as in the 2D experiment[6]), restricting to the coherent dynamics (that is relaxation between the vibronic components is not included). When calculating the SE components shown in Figure 5 we assume the low-temperature limit, and we do not include disorder. The intensities of the SE components oscillating with the frequency $\Omega_{osc}=\omega_b-\omega_{b'}$ are shown in the $\{\omega_\tau, \omega_t\}$ plane, where $\omega_\tau=\omega_{b'}-\omega_{c=1}$ is the excitation frequency (corresponding to transition from the lowest c=1 level of the ground state to the exciton-vibrational level b' of the excited-state manifold), and $\omega_t=\omega_b-\omega_c$ is the emitting frequency (corresponding to emission from the excited state b to the level c of the ground state).

The coherence between the b and b' states (contributing to the SE oscillations) can have purely vibrational, mixed exciton-vibrational, or predominantly excitonic origin. The excitonic coherence produces two symmetric oscillating SE peaks (exciton duplets) due to excitation of b or b' ZPL (from c=1) followed by creation of the b-b' population with subsequent emission to the c=1 level. The vibrational and mixed coherences produce four oscillating SE peaks (quadruplets). Two additional peaks appear due to depopulation of the b-b' coherence to the first c=1 or second c=2-5 degenerate sublevel of the ground state).

The degree of exciton mixing P_{nm} between the sites n,m present in the b-b' coherence can be defined as:

$$P_{nm}(b,b') = \left| \sum_a C^e_{n,ab} C^e_{m,ab'} \right| + \left| \sum_a C^e_{m,ab} C^e_{n,ab'} \right| \qquad (4)$$

The maximum value P_{nm}=1 corresponds to a pure exciton mixing with complete delocalization over the two sites. For a purely vibrational coherence without any exciton mixing P_{nm} is equal to zero.

Calculation of the 2DFT maps.

Figure 6 is an example of quantitative modeling, where we try to reproduce the experimentally measured 2D frequency maps. The third-order polarization needed to obtain the 2D-echo has been calculated using an expansion of the Liouville equation for the reduced density matrix up to third order with respect to the external field (similar to the expansion shown in ref. 26). The 2D frequency maps can be obtained after Fourier transformation of the 2D responses with respect to the population time. Such a transformation yields a series of two-dimensional maps on the $\{\omega_\tau, \omega_t\}$ plane (2DFT maps), showing the components of the 2D spectra oscillating at a certain frequency.[6] The calculated 2DFT maps include all the components, that is, SE, ground-state bleach (GSB) and excited-state absorption (ESA) averaged over disorder and over all possible orientations of the complex. Initial populations of the ground-state sublevels correspond to a Boltzmann distribution at 77K. In the excited state we restrict to coherent dynamics, that is we do not consider the relaxation dynamics between different vibronic states. Without relaxation we cannot calculate the homogeneous broadening, so the line shapes are obtained using some phenomenological line width.

The example shown in Figure 5 demonstrates that coupling to just one vibrational mode produces a rich manifold of 2D components with different oscillating frequencies (even for a single realization of the disorder). Obviously, the 2DFT map at a certain frequency Ω_{osc} will contain a superposition of components originating from the coupling to many modes with different vibrational frequencies Ω. Unfortunately, including of coupling to several modes is too complicated numerically. In our simplified model we restrict to coupling to just one mode. In order to collect a representative set of oscillating components in the calculated 2D response, we have repeated the calculation using different values of the vibrational frequency, taken consequently from some manifold. In such a single-mode approach we do not consider the combined effect of many modes, assuming it to be negligible for small Huang-Rhys factors ($\Delta^2/2 \ll 1$). Notice that in our recent study[11] this approach allowed us to explain quantitatively the 2DFT maps for the dimeric B820 subunit of the bacterial LH1 antenna. In the present modeling we use the manifold of vibrational modes with frequencies $\Omega=\{120\ \ 265\ \ 340\ \ 518\ \ 740\ \ 1140\}$ cm^{-1}, and displacements $\Delta=\{0.68\ \ 0.80\ \ 0.68\ \ 0.57\ \ 0.54\ \ 0.57\}$. These parameters correspond to the experimental spectral density used in our previous modeling of the PSII-RC based on Redfield theory.[4,6,25] After calculating the 2D spectra (averaged over disorder and orientations) with contributions from all these frequencies (calculated sequentially and added) we perform a Fourier transformation of the resulting coherent dynamics and obtain the 2DFT maps for the 120, 340, and 740 cm^{-1} components. Notice that these maps contain contributions from oscillating components within a window of about 20 cm^{-1} corresponding to a phenomenological decay of the coherences with a time constant of 0.5 ps as supposed in our modeling. The thus calculated maps are compared with the measured ones in Figure 6.

To estimate the contribution of the exciton mixing in the apparent quantum beats the $P_{nm}(b,b')$ values should be weighed with the amplitudes of the corresponding SE components (normalized to the maximal value of the total SE signal). Summation of the weighted $P_{nm}(b,b')$ values over all pairs of pigments (n,m) and all the components (b,b') within some $\{\omega_\tau, \omega_t\}$ region allows to estimate the total degree of exciton mixing P_{coh} for the main peaks of the 2DFT maps (located on- or below diagonal). We do not analyze the weak peaks above diagonal, where the (b,b') coherences contribute to overlapping (and partially compensating each other) SE and ESA components.

5. Conclusions

We conclude that the electron-vibrational resonances largely present in the PSII-RC create nontrivial effects by coherently mixing the relevant electronic states. In the case of exciton states the resonant vibrations produce directed energy flow to one of the two possible primary donors. In the case of a resonance with the exciton-CT or CT-CT gap, the coherent mixing of vibrational sublevels of these states gives rise to highly efficient charge separation. It is important that such kind of coherent mixing occurs within eigenstates, and therefore, it increases the rate of energy and electron transfers along a particular direction not only upon coherent excitation, but also in natural light-harvesting and charge separation.

The 2D photon echo allows a visualization of different types of the coherent mixing in the form of oscillatory features with specific signatures on the 2DFT frequency maps. Using this method we have found a variety of coherences in the PSII-RC, including predominantly excitonic, purely vibrational ones, and exciton-vibrational (vibronic) coherences with low or high degree of exciton mixing (depending on how far is the vibrational frequency from the exciton splitting). Finally, we propose that the matching of the frequencies of the most intense intra-molecular vibrational modes with the main exciton (and exciton-CT) splittings is, most probably, not just a coincidence, but on the contrary it reflects a fundamental principle of optimization of energy conversion in photosynthesis.

Acknowledgements

V.I.N. was supported by the visitors grant from the Dutch Foundation for Basic Research (NWO, Grant No. 040.11.428) and by the Russian Foundation for Basic Research (Grant No. 15-04-02136); E. R. and R. v. G. were supported by the VU University Amsterdam, the Laserlab-Europe Consortium, the TOP grant (700.58.305) from the Foundation of Chemical Sciences part of NWO, the advanced investigator grant (267333, PHOTPROT) from the European Research Council, and by the EU FP7 project PAPETS (GA 323901). R.v.G. gratefully acknowledges his Academy Professor grant from the Netherlands Royal Academy of Sciences (KNAW).

References

1 R. van Grondelle, J. P. Dekker, T. Gillbro and V. Sundström, *Biochim. Biophys. Acta - Bioenerg.*, 1994, **1187**, 1–65.
2 Blankenship, R. E. *Molecular Mechanisms Of Photosynthesis*. (Blackwell Science Ltd, Oxford, 2002).

3 R. van Grondelle and V. I. Novoderezhkin, *Phys. Chem. Chem. Phys.*, 2006, **8**, 793–807.

4 V. I. Novoderezhkin, J. P. Dekker, R. van Grondelle, *Biophys. J.* 2007, **93**, 1293-1311.

5 E. Romero, B. A. Diner, P. J. Nixon, W. J. Coleman, J. P. Dekker and R. van Grondelle, *Biophys. J.* 2012, **103**, 185-194.

6 E. Romero, R. Augulis, V. I. Novoderezhkin, M. Ferretti, J. Thieme, D. Zigmantas, and R. van Grondelle, *Nat. Phys.* 2014, **10** , 676-682.

7 G. S. Schlau-Cohen, J. M. Dawlaty, and G. R. Fleming, *IEEE J. Sel. Top. Quant. Electron.* 2012, **18,** 283-295.

8 G. S. Engel, T. R. Calhoun, E. L. Read, T.-K. Ahn, T. Mancal, Y.-C. Cheng, R. E. Blankenship and G. R. Fleming, *Nature*, 2007, **446**, 782–786.

9 E. Collini, C. Y. Wong, K. E. Wilk, P. M. G. Curmi, P. Brumer and G. D. Scholes, *Nature*, 2010, **463**, 644–647.

10 J. M. Anna, J. D. Scholes, and R. van Grondelle, *BioScience* 2014, **64**, 14-25.

11 M. Ferretti, V. I. Novoderezhkin, E. Romero, R. Augulis, A. Pandit, D. Zigmantas and R. van Grondelle, *Phys. Chem. Chem. Phys.* 2014, **16**, 9930-9939.

12 F. D. Fuller, J. Pan, A. Gelzinis, V. Butkus, S. Seckin Senlik, D. E. Wilcox, C. F. Yocum, L. Valkunas, D. Abramavicius and J. P. Ogilvie, *Nat. Chem.* 2014, **6**, 706-711.

13 A. Kolli, A. Nazir and A. Olaya-Castro, *J. Chem. Phys.* 2011, **135**, 154112.

14 N. Christensson, H. F. Kauffmann, T. Pullerits and T. Mančal, *J. Phys. Chem. B*, 2012, **116**, 7449-7454.

15 A. W. Chin, S. F. Huelga and M. B. Plenio, *Philos. Trans. A. Math. Phys. Eng. Sci.*, 2012, **370**, 3638-3657.

16 A. Kolli, E. J. O'Reilly, G. D. Scholes and A. Olaya-Castro, *J. Chem. Phys.*, 2012, **137**, 174109.

17 A. W. Chin, J. Prior, R. Rosenbach, F. Caycedo-Soler, S. F. Huelga and M. B. Plenio, *Nat. Phys.*, 2013, **9**, 113–118.

18 V. Tiwari, W. K. Peters and D. M. Jonas, *Proc. Natl. Acad. Sci. U. S. A.*, 2013, **110**, 1203-1208.

19 V. Butkus, D. Zigmantas, L. Valkunas and D. Abramavicius, *Chem. Phys. Lett.*, 2012, **545**, 40-43.

20 F. Fassioli, A. Olaya-Castro and G. D. Scholes, *J. Phys. Chem. Lett.*, 2012, **3**, 3136-3142.

21 E. J. O'Reilly and A. Olaya-Castro, *Nat. Commun*., 2014, **5**, 3012.

22 J. M. Womick and A. M. Moran, *J. Phys. Chem. B*, 2011, **115**, 1347-1356.

23 S. L. S. Kwa, W. R. Newell, R. van Grondelle and J. P. Dekker, *Biochim. Biophys. Acta,* 1992, **1099**, 193-202.

24 E. Romero, I. H. M. van Stokkum, V. I. Novoderezhkin, J. P. Dekker and R. van Grondelle, *Biochemistry,* 2010, **49**, 4300-4307.

25 V. I. Novoderezhkin, E. Romero, J. P. Dekker and R. van Grondelle, *ChemPhysChem,* 2011, **12**, 681-688.

26 V. I. Novoderezhkin, A. G. Yakovlev, R. van Grondelle and V. A. Shuvalov, *J. Phys. Chem. B*, 2004, **108**, 7445-7457.

27 B. P. Fingerhut, W. Zinth and R. de Vivie-Riedle, *Chem. Phys. Lett.,* 2008, **466**, 209–213.

28 F. Fassioli, R. Dinshaw, P. C. Arpin and G. D. Scholes, *J. R. Soc. Interface* 2014, **11**, 20130901.

29 D. Abramavicius and L. Valkunas, *Photosynth. Res*., 2015, doi: 10.1007/s11120-015-0080-6.

30 P. Rebentrost, M. Mohseni and A. Aspuru-Guzik, *J. Phys. Chem. B,* 2009, **113**, 9942–9947.

31 C. Kreisbeck, T. Kramer and A. Aspuru-Guzik, *J. Phys. Chem. B*, 2013, **117**, 9380−9385.

32 C. Kreisbeck and T. Kramer, *J. Phys. Chem. Lett.,* 2012, **3**, 2828−2833.

33 J. M. Jean and G. R. Fleming, *J. Chem. Phys.,* 1995, **103**, 2092-2101.

34 A. Chenu, P. Malý, and T. Mančal, *Chem. Phys.,* 2014, **439**, 100-110.

35 K. M. Pelzer, T. Can, S. K. Gray, D. K. Morr and G. S. Engel, *J. Phys. Chem. B,* 2014, **118**, 2693−2702.

36 G. Raszewski, W, Saenger and T. Renger, *Biophys. J.* 2005, **88**, 986-998.

37 G. Raszewski, B. A. Diner, E, Schlodder and T. Renger, *Biophys. J.* 2008, **95**, 105-119.

38 I. V. Shelaev, F. E. Gostev, M. I. Vishnev, A. Ya. Shkuropatov, V. V. Ptushenko, M. D. Mamedov, O. M. Sarkisov, V. A. Nadtochenko, A. Yu. Semenov and V.A. Shuvalov, *J. Photochem. Photobiol. B: Biology,* 2011, **104**, 44-50.

39 K. L. M. Lewis, F. D. Fuller, J. A. Myers, C. F. Yocum, S. Mukamel, D. Abramavicius and J. P. Ogilvie, *J. Phys. Chem. A,* 2013, **117**, 34-41.

40 A. Gelzinis, L. Valkunas, F. D. Fuller, J. P. Ogilvie, S. Mukamel and D. Abramavicius, *New J. Phys.,* 2013, **15**, 075013.
41 L. Zhang, D.-A. Silva, H. Zhang, A. Yue, Y. Yan and X. Huang, *Nat. Commun.,* 2014, **5**, 4170.
42 T. Förster, in *Modern Quantum Chemistry, Part III. B. Action of Light and Organic Crystals*, ed. Sinanoğlu, Academic Press, New York, 1965, pp. 93‑137.
43 V. Butkus, D. Zigmantas, D. Abramavicius and L. Valkunas, *Chem. Phys. Lett.,* 2013, **587**, 93–98.
44 J. M. Jean, *J. Chem. Phys.,* 1994, **101**, 10464-10473.
45 D. Egorova, M. Thoss, H. Wang, and W. Domcke, *J. Chem. Phys.,* 2003, **119**, 2761-2773.
46 D. Egorova and W. Domcke, *J. Photochem. Photobiol A: Chemistry,* 2004, **166**, 19-31.
47 M. Tanaka and Y. Tanimura, *J. Phys. Soc. Jpn.,* 2009, **78**, 073802.
48 Y. Tanimura, *J. Chem. Phys.,* 2012, **137**, 22A550.

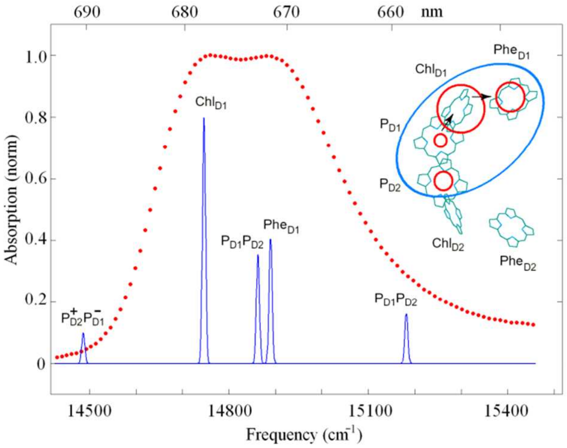

Figure 1. Arrangement of the 6 core pigments of the PSII-RC. Red circles show the disorder-averaged participation of these pigments in the lowest exciton state (according to our model[4]). The four pigments of the active branch included into the reduced 4-state model are encircled by cyan. Arrows show a direction of electron transfer. The exciton structure emerging from such a 4-state model (absorption stick spectrum given by pure electronic transitions without phonons and disorder) is shown by blue. The labels near the peaks indicate the pigments giving the predominant contribution to the corresponding exciton state. For comparison we also include the unperturbed zero-phonon line corresponding to a primary CT state $P_{D2}^{+}P_{D1}^{-}$, that is about 260 cm^{-1} red-shifted from the lowest exciton state.[4] The 77K absorption measured for the isolated PSII-RC[23] is shown as a reference (red points).

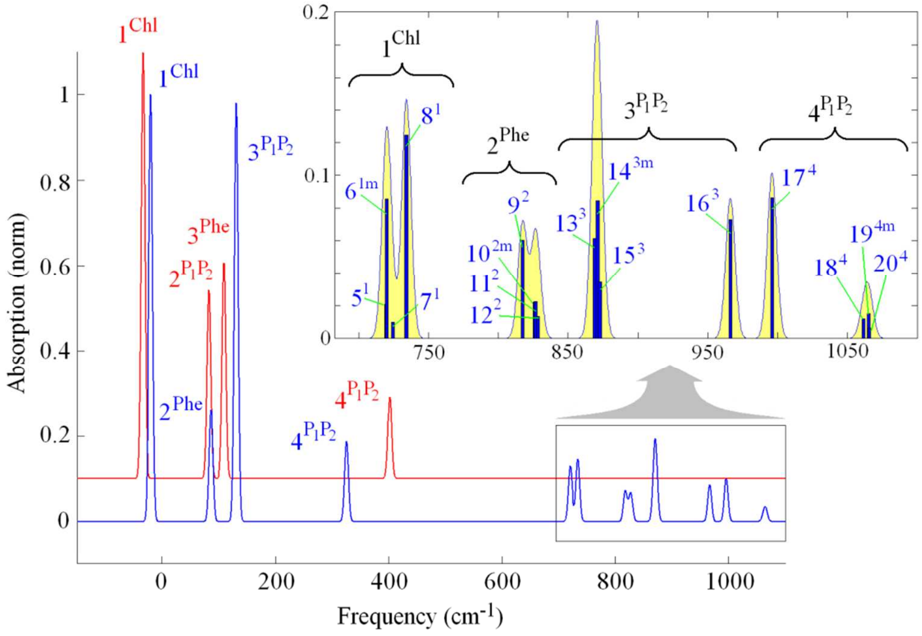

Figure 2. Absorption spectrum (normalized) corresponding to the coupling of electronic excitations to a single vibrational mode with Ω=740 cm^{-1} and displacement Δ=0.9 (blue). The spectrum without coupling to vibrations (Δ=0) is shown for comparison with a vertical shift of 0.1 (red). We calculate the stick spectra without homogeneous broadening and without disorder. Each component has a Gaussian line shape with a FWHM of 8 cm^{-1}. The spectrum is calculated for the low-temperature limit, when absorption occurs only from the lowest vibrational level of the ground state. Frequency is counted from the ZPL of the red-most pigment (Chl_{D1}). Inset shows the vibronic components of the Δ=0.9 spectrum in the 680-1050 cm^{-1} region. Labeling is explained in the text.

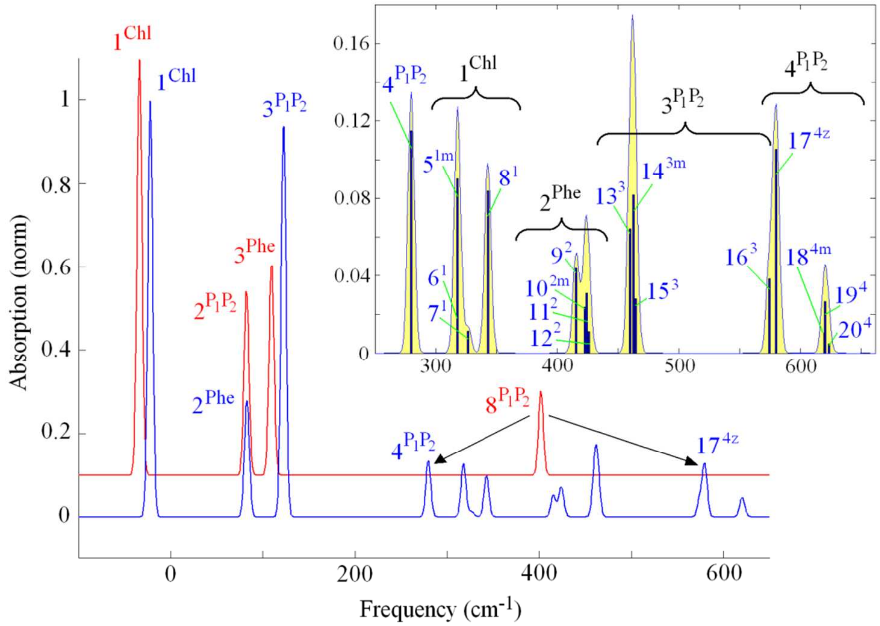

Figure 3. The same as in Figure 2, but with Ω=340 cm^{-1}. Black arrows show how the dipole strength of the upper exciton origin is shared between two levels in the case of coupling to a resonant vibration. Each component has a Gaussian line shape with full width at half maximum (FWHM) of about 6 cm^{-1}. Inset shows the vibronic components of the Δ=0.9 spectrum in the 250-665 cm^{-1} region.

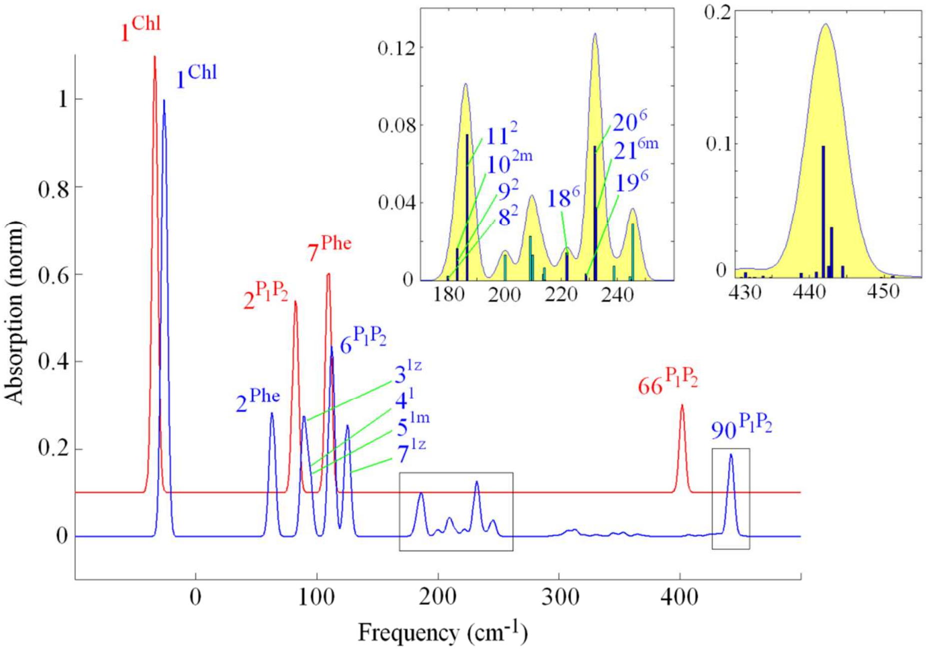

Figure 4. The same as in Figure 2, but with Ω=120 cm^{-1}. Each component has a Gaussian line shape with FWHM of about 5 cm^{-1}. First insert shows vibronic components of the Δ=0.9 spectrum in the 170-260 cm^{-1} region, including the one-quantum sublevels (blue bars, labeled as 8^2-11^2 and 18^6-20^6) and two-quantum sublevels (green bars, non-labeled). The second inset shows the structure of the band containing the higher exciton origin mixed with high-order vibrational sublevels of lower exciton states in the 430-455 cm^{-1} regions.

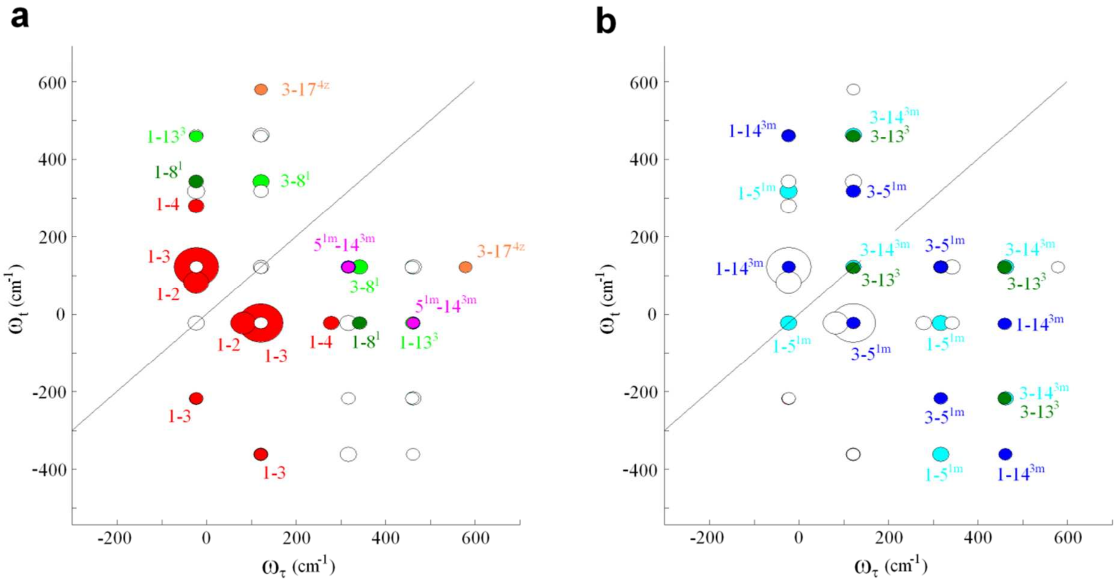

Figure 5. Intensities of the oscillating SE components of the rephasing 2D photon echo calculated for Ω=340 cm^{-1} and Δ=0.9 in the low-temperature limit and without disorder. The positions of the most intense components are shown as a function of excitation ω_τ and emission ω_t frequencies. The area of the circles is proportional to the intensity of that component in the rephrasing 2D photon echo spectra; the colors indicate 7 different types of coherences described in the text, that is type 1 (red), 2 (orange), 3 (magenta), 4 (green), 5 (dark green), 6 (cian), 7 (blue); the numbers near the components correspond to the *b*-*b'* indices (note that we use the same label for *b*-*b'* and *b'*-*b* coherences), specifying which pair of levels is coherently excited (superscripts are the same as in Figure 3, but we drop superscripts for true ZPLs, labeled as 1, 2, 3, or 4). Intensities are calculated by averaging over all possible orientations of the complex supposing parallel polarization of the four pulses (as in the 2D-echo experiment[6]). The relaxation between the exciton-vibrational levels is not included. Only the components with Ω_{osc} >50 cm^{-1} are shown. **(a)** Marked and labeled are only the SE duplets produced by pure exciton coherences (types 1-3) and mixed coherences with significant exciton contribution (types 4 and 5). **(b)** Marked and labeled are only the SE quanduplets produced by purely vibrational coherences (type 6) and by mixed coherences with small exciton contribution (types 5 and 7). Note that mixed coherences both with either large or small exciton contributions oscillate at a frequencies different from Ω=340 cm^{-1}.

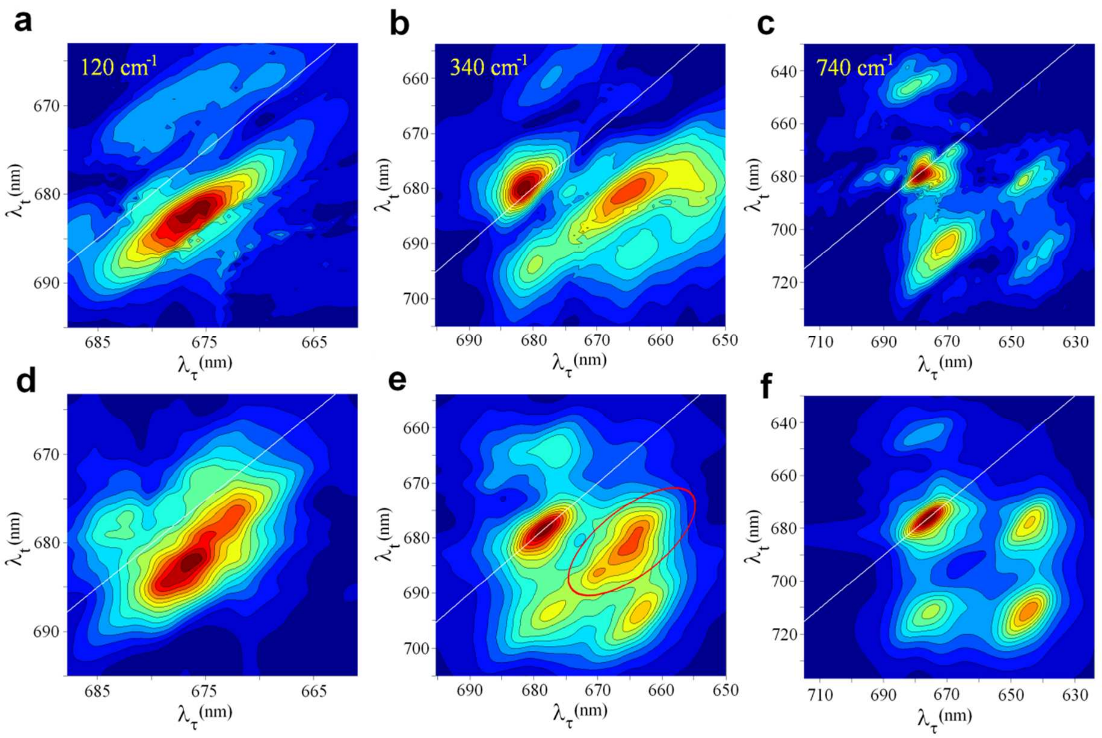

Figure 6. Measured (**a-c**) and calculated (**d-f**) 2DFT maps at 120, 340, and 740 cm^{-1}, respectively. The maps are shown as a function of excitation λ_τ and emission λ_t wavelengths. The diagonal ($\lambda_\tau = \lambda_t$) is shown by white line. The experimental maps correspond to the real rephasing 2D kinetics measured for isolated PSII-RC at 77K.[6] The calculated maps are obtained from the disorder-averaged and orientation-averaged 2D responses corresponding to the coherent dynamics within the active branch of the PSII-RC (containing P_{D1}, P_{D2}, Chl_{D1}, and Phe_{D1}). In the calculated 340 cm^{-1} map the peak corresponding to exciton-vibrational coherence with a significant degree of exciton mixing has been encircled.

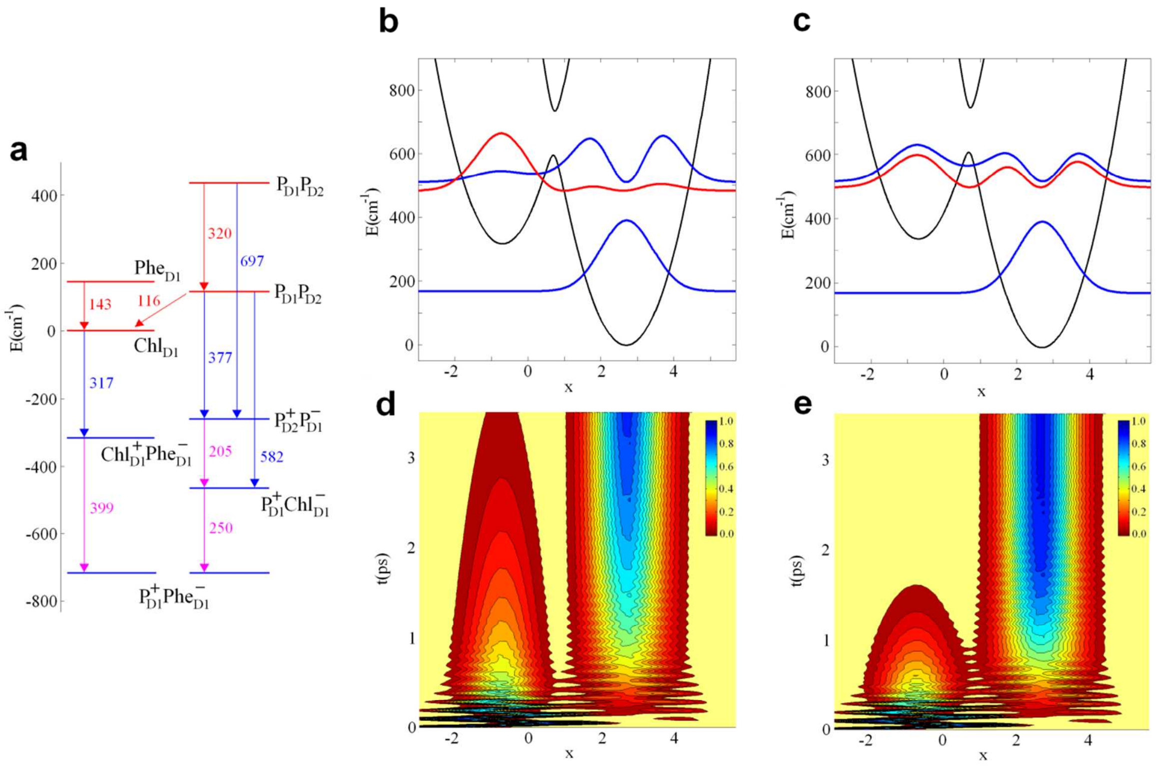

Figure 7. Energy level scheme and the role of resonant vibrations. **(a)** Energy level scheme for the excited states and radical pairs of the PSII-RC. Positions of the ZPLs of the four exciton states of our 4-state model (red) are shown together with the ZPLs of radical pairs (blue). We show the unperturbed values of the ZPLs (that is without taking into account the disorder and phonons), counting from the ZPL of the lowest exciton state localized at Chl_{D1}. The ZPL positions of the radical pairs are taken from our previous models.[4,25] Arrows show the channels of energy transfers (red), electron transfers from primary donors to primary CT states (blue), and transfers between CTs (magenta). The numbers indicate the energy gaps corresponding to these transfers (in order to compare them with the vibrational frequencies). **(b)** The shape of the three lowest vibronic wavefunctions (red and blue lines) in the case of a 340 cm^{-1} mode coupled to the exciton and CT states separated by a gap of 320 cm^{-1}. Displacement Δ is -0.7 and 2.7 for the exciton and CT states, respectively. Coupling between the diabatic electronic states is M=70 cm^{-1}. Potential surfaces for the two mixed states are shown by black lines. **(c)** The same as in **b**, but in the case of resonance, that is for the energy gap of 340 cm^{-1}. **(d)** Dynamics of the vibrational wavepacket after impulsive excitation of the exciton state coupled to the CT state (parameters are the same as in frame **b**). Initial excited-state wavepacket corresponds to transitions from the ground state potential (with the displacement of -2.4 (not shown)) induced by absorption of a delta-pulse. Dynamics is calculated using the Redfield theory in the exciton-vibrational basis at 77K, as described in the text. (**e**) The same as in **d**, but for resonant configuration shown in frame **c**.